



# CHORUS

This is the accepted manuscript made available via CHORUS. The article has been published as:

## Spin rectification for collinear and noncollinear magnetization and external magnetic field configurations

Y. Huo, L. H. Bai, P. Hyde, Y. Z. Wu, and C.-M. Hu

Phys. Rev. B **91**, 174430 — Published 26 May 2015

DOI: [10.1103/PhysRevB.91.174430](https://doi.org/10.1103/PhysRevB.91.174430)

# Spin rectification for collinear and non-collinear magnetization and external magnetic field configurations

Y. Huo,<sup>1,2,\*</sup> and L. H. Bai,<sup>2</sup> P. Hyde,<sup>2</sup> Y. Z. Wu,<sup>1</sup> and C.-M. Hu<sup>2</sup>

<sup>1</sup> *Department of Physics, State Key Laboratory of Surface Physics and Collaborative Innovation Center of Advanced Microstructures, Fudan University, Shanghai 200433, China and*

<sup>2</sup> *Department of Physics and Astronomy, University of Manitoba, Winnipeg, Manitoba R3T 2N2, Canada*

Spin rectification in a single crystal Fe/Au/Fe sandwich is electrically detected for collinear and non-collinear magnetization and external magnetic field configurations. The line shape, line width and signal polarity are analyzed. The spin rectification theory has been much extended by taking the magneto-crystalline anisotropy and shape anisotropy into account, which explains non-collinear resonances and agrees very well with experimental data. Thus, a comprehensive understanding of spin rectification in ferromagnetic metal is demonstrated in this work.

PACS numbers: 67.30.hj, 76.50.+g, 75.30.Gw, 75.47.-m

A decade ago, spin dynamics in ferromagnetic materials was electrically detected via the spin diode effect in magneto tunnel junctions<sup>1,2</sup> and the bolometric effect in thin films<sup>3,4</sup>, which triggered a rapid development. Later, more methods were developed, such as the spin pumping effect<sup>5</sup>, the (inverse) spin hall effect<sup>6</sup> and the spin rectification effect (SRE)<sup>7-23</sup>. As detailed in two recent review articles of spin rectification<sup>24,25</sup>, the SRE dominates the electrical voltage induced by ferromagnetic resonance (FMR) in a variety of ferromagnetic metals. A precessing magnetization leads to a periodically changing resistance through magneto-resistance. The periodically changing resistance couples with the microwave current flowing inside and generates a DC voltage, this is the SRE<sup>10</sup>. Such a method became the most popular method in electrical detection of FMR because of its high sensitivity, simple sample structure, and experimental set-up. It was applied to different materials and structures with accurate agreement between theory and experimental results on both line shape and line width<sup>24,25</sup>. Such line shape analysis is useful for distinguishing spin rectification from spin pumping and the inverse spin hall effect<sup>13,20,21</sup>. Line width is also important for determining additional damping due to spin pumping as well as the intrinsic Gilbert damping<sup>10,26,27</sup>. Almost all the previous studies of line shape and line width were performed in a collinear case where the magnetization is aligned parallel with the external magnetic field. However, in ferromagnetic thin films, the magnetization orientates along an effective field direction rather than the external magnetic field direction, especially when the internal magnetic fields, such as the magnetic anisotropy field and demagnetization field, are comparable to the external magnetic field. In such a non-collinear case of the magnetization and the external magnetic field, line shape and line width analyses of spin rectification haven't been systematically studied yet.

In this work, we experimentally studied the line shape and line width of spin rectification in a non-collinear case for a sample with strong anisotropy. We also extend spin

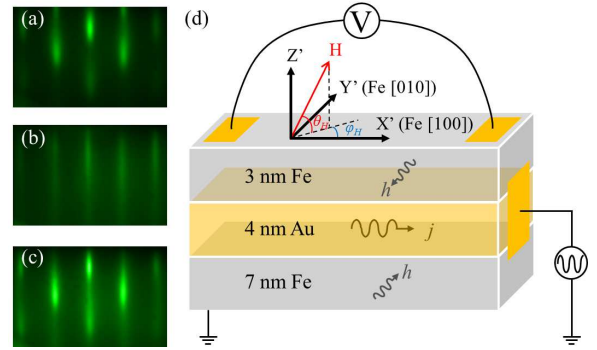


FIG. 1. RHEED patterns with the electron beam  $e^-$  along MgO  $\langle 100 \rangle$  of (a) Fe (7 nm)/MgO, (b) Au (4 nm)/Fe (7 nm)/MgO, and (c) Fe (3 nm)/Au (4 nm)/Fe (7 nm)/MgO. (d) a sketch of measurement geometry.

rectification theory from the collinear case into the non-collinear case by considering all anisotropy effects. Thus, we present a comprehensive understanding of spin rectification in a metallic system.

To achieve a system with strong anisotropy, we designed an ultra-thin single crystal Fe/Au/Fe sandwich on a MgO (001) substrate by using molecular beam epitaxy in a ultra high vacuum chamber. The substrate was cleaned by annealing at 680°C for 45 minutes. Then, a 7-nm-thick Fe layer was prepared at room temperature and annealed at 250°C for 3 minutes until high crystalline quality was achieved as indicated by a sharp reflection of high-energy electron diffraction (RHEED) pattern, as shown in Fig. 1 (a). A 4-nm-thick Au layer was then epitaxially deposited at room temperature. A 3-nm-thick of Fe layer was then epitaxially deposited. Further, a 5-nm-thick MgO layer was deposited on top for protection. The RHEED patterns shown in Fig. 1(a)-(c) indicate the smoothness of each layer surface and the high crystalline quality of the sample. In addition to the shape anisotropy, the single crystal Fe ultra-

thin film on MgO (001) has a strong in-plane magneto-crystalline anisotropy with the easy axis along the Fe [100] and the hard axis along Fe [110]<sup>28</sup>, and the two Fe layers with different thickness will have different magnetic anisotropies<sup>29,30</sup>, which have all been confirmed by our measurements. Both magneto-crystalline anisotropy and shape anisotropy in the Fe/Au/Fe sandwich allow us to study non-collinear spin rectification.

As shown in Fig. 1(d), the tri-layer sample was patterned into a strip along the Fe [100] easy axis with the dimensions of  $20 \mu\text{m} \times 3 \text{mm}$  using standard photo lithography. A microwave was applied into the strip directly, and most microwave current flows inside of the Au layer due to its high conductivity. Thus, the microwave magnetic field on the bottom layer has a phase shift of  $\pi$  with that in the top layer. The microwave was modulated with a frequency of 8.33 kHz. Voltage was measured along the strip using a lock-in technique. An external magnetic field  $\mathbf{H}$  was applied to the strip with the orientation defined in Fig. 1(d). Spin rectification voltage was measured by sweeping the external magnetic field at a fixed microwave frequency. In this work, microwave power is 100 mW. **Before taking systematic measurements, we have checked the magnetization coupling and the spin dynamic coupling between the two Fe layers. When FMR occurs in both Fe layers in our sample, we observed a simple crossing in the  $\omega - H$  dispersion of FMR for 3 nm and 7 nm Fe. Usually, the magnetic coupling between two FM layers can induce an anti-crossing in the  $\omega - H$  dispersion<sup>31-34</sup>, so the missing of the anti-crossing in our measurement indicates that magnetic coupling in our sample can be ignored. Moreover, around the crossing, no significant linewidth reduction<sup>35</sup> or amplitude enhancement<sup>22</sup> of the resonance peaks is observed, and then the spin dynamic coupling can be considered too weak to influence the FMR of both Fe layers. Thus, we can consider the two Fe layers as two independent FM layers without the magnetic coupling and the spin dynamic coupling. We have carefully checked the sample at the special geometry<sup>20</sup> for measuring the pure spin pumping signal, which is ignorably small compared to that of spin rectification. Thus, we were allowed to study the line shape, line width, and polarity of the pure spin rectification signal in both collinear and non-collinear cases.**

Figure 2 shows the results when  $\mathbf{H}$  is applied near Fe [110] direction in the film plane, which is the hard axis of four-fold magneto crystalline anisotropy. Fig. 2(a) shows a sketch of an in-plane configuration measurement with  $\varphi_H \approx 45^\circ$  and  $\vartheta_H = 0^\circ$ . For this case, when  $\mathbf{H}$  is larger than the saturation field, the magnetization  $\mathbf{M}$  will lie almost parallel to the  $\mathbf{H}$  direction, while if  $\mathbf{H}$  is smaller than the saturation field,  $\mathbf{M}$  will be pulled out of the collinear configuration, and the relative angle between  $\mathbf{M}$  and  $\mathbf{H}$  is determined by the competition between the Zeeman energy and the four-fold magneto-crystalline anisotropy energy. Fig. 2(b) shows an  $\omega - \mathbf{H}$  dispersion plot with the normalized rectification

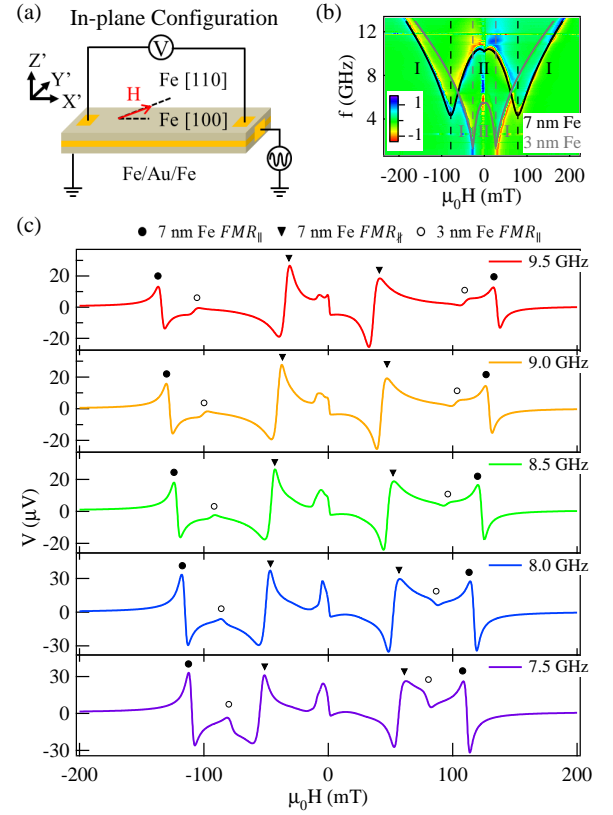


FIG. 2.  $V_{SR}$  measurement with  $\mathbf{H}$  along hard axis Fe [110] in plane. (a) The sketch of the in-plane configuration measurement; (b)  $\omega - \mathbf{H}$  dispersion image plot, the grey solid line is the fitting curve of 3 nm Fe, and the black solid line is the fitting curve of 7 nm Fe; both dispersion curves have two branches: branch I is  $FMR_{\parallel}$  branch, and branch II is  $FMR_{\perp}$  branch. (c) Typical curves in the in-plane configuration, solid circles ( $\bullet$ ) indicate peaks belong to  $FMR_{\parallel}$  branch in 7 nm Fe, solid triangles ( $\blacktriangledown$ ) indicate peaks belong to  $FMR_{\perp}$  in 7 nm Fe, hollow circles ( $\circ$ ) indicate peaks belong to  $FMR_{\parallel}$  in 3 nm Fe.

voltage amplitude mapped into a rainbow color scale. The dispersion curves can be calculated by solving the Landau-Lifshitz-Gilbert (LLG) equation<sup>28</sup>. By fitting with the measurement data, we got four-fold magnetic anisotropy field  $\mu_0 H_1 = 73 \text{ mT}$ , the effective magnetization  $\mu_0 M_{eff} = 1.7 \text{ T}$  (black solid line) and  $\mu_0 H_1 = 26 \text{ mT}$ ,  $\mu_0 M_{eff} = 1.4 \text{ T}$  (grey solid line) for two Fe layers. By the Fe-thickness dependence of anisotropy in Fe/MgO (001) systems<sup>29,30</sup>, we can identify the dispersion curve traced by the black solid line as originating from the 7 nm Fe layer and the curve traced by the grey solid line as originating from the 3 nm Fe layer. These two dispersion curves cross at  $\mu_0 H = \pm 65 \text{ mT}$ , the independence of the two dispersion curves near the crossing indicates the coupling between the two FM layers is ignorable for the reasons discussed in the previous paragraph. Both the  $\omega - \mathbf{H}$  dispersion curves have two branches, as shown in Fig. 2(b). In branch I, the resonance field increases with the frequency, here  $\mathbf{H}$  is larger than the satura-

tion field and thus  $\mathbf{M} \parallel \mathbf{H}$ ; we define the resonance in this situation as  $FMR_{\parallel}$  branch. In branch II, the resonance field decreases as the frequency increases, here  $\mathbf{H}$  is smaller than the saturation field and thus  $\mathbf{M} \nparallel \mathbf{H}$ ; we define the resonance in this situation as  $FMR_{\nparallel}$  branch. Fig. 2(c) shows some typical curves measured in this configuration at various microwave frequencies between 7.5 GHz and 9.5 GHz. **At resonance, the SRE curves can be separated into the anti-symmetric Lorentz shape and the Lorentz shape, but the overall curves are dominated by the anti-symmetric Lorentz lineshape, which indicates the relative phase  $\Phi$  between the microwave field  $\mathbf{h}$  and microwave current  $\mathbf{j}$  almost has the value of the integer number of  $\pi$ <sup>14</sup>.** In addition to the rectification voltage observed at the FMR fields of the 3 nm Fe and 7 nm Fe, a non-resonant rectification signal is observed around  $\mu_0 H=0$ , and this signal can be attributed to the spin rotation while the magnetic field reverses, as discussed in Ref.<sup>36</sup>. In this paper we shall focus our study only on the resonance rectification voltage. From Fig. 2(c), we summarize the main features of the SRE measured in the in-plane configuration by the following Eqs. (1): (a) all voltage signals change their polarity when the applied magnetic field reverses; (b) the voltage polarity in the 7 nm Fe  $FMR_{\parallel}$  branch is opposite to the polarity in the 3 nm Fe  $FMR_{\parallel}$  branch; (c) the voltage polarity in  $FMR_{\parallel}$  branch is opposite to the polarity in  $FMR_{\nparallel}$  branch.

At  $\varphi_H \approx 45^\circ, \vartheta_H = 0^\circ$  :

$$V(H) = -V(-H) \quad (1a)$$

$$\frac{V_{Fe7}}{|V_{Fe7}|} = -\frac{V_{Fe3}}{|V_{Fe3}|} \quad (1b)$$

$$\frac{V_{FMR_{\parallel}}}{|V_{FMR_{\parallel}}|} = -\frac{V_{FMR_{\nparallel}}}{|V_{FMR_{\nparallel}}|} \quad (1c)$$

Eq. (1a) is in agreement with the studies in the literature<sup>10,14,20</sup>, and Eq. (1b) describes the polarity difference in the two Fe layers due to the phase shift of the microwave field. Eq. (1c) indicates that in the in-plane configuration the polarity of  $V_{SR}$  changes its sign for the case where  $\mathbf{M}$  and  $\mathbf{H}$  are non-collinear. Shown in Fig. 2(c), the resonance peaks in the  $FMR_{\nparallel}$  branch are much broader than those in the  $FMR_{\parallel}$  branch.

In addition to magneto-anisotropy, the shape anisotropy is also able to affect the relative angle between  $\mathbf{M}$  and  $\mathbf{H}$ . Fig. 3 shows the results when  $\mathbf{H}$  is applied almost perpendicular to the film plane, with Fig. 3(a) showing a sketch of an out-of-plane measurement configuration with  $\varphi_H = 0^\circ$  and  $\vartheta_H \approx 90^\circ$ . In this configuration,  $\mathbf{M} \parallel \mathbf{H}$  for  $\mathbf{H}$  is larger than the saturation field, and  $\mathbf{M} \nparallel \mathbf{H}$  for  $\mathbf{H}$  is smaller than the saturation field. The relative angle between  $\mathbf{M}$  and  $\mathbf{H}$  is determined by the competition between the Zeeman energy and shape anisotropy energy. **In our system, the effective shape anisotropy field is  $\mu_0 M_{eff} = 1.7 T$  for 7 nm Fe, and  $\mu_0 M_{eff} = 1.4 T$  for 3 nm Fe.** Fig. 3(b) shows an  $\omega$ - $\mathbf{H}$  dispersion plot, with normalized rectification voltage amplitude mapped into a rainbow

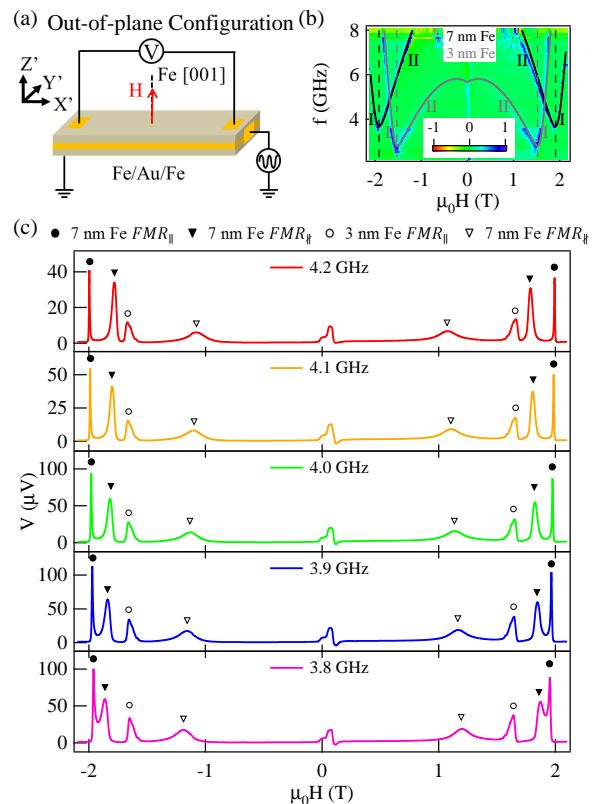


FIG. 3.  $V_{SR}$  measurement with  $\mathbf{H}$  pointing out of the film plane. (a) The sketch of the out-of-plane configuration measurement; (b)  $\omega$ - $\mathbf{H}$  dispersion image plot, the grey solid line is the fitting curve of 3 nm Fe, and the black solid line is the fitting curve of 7 nm Fe; both dispersion curves have two branches: branch I is  $FMR_{\parallel}$  branch, and branch II is  $FMR_{\nparallel}$  branch. (c) Typical curves in out-of-plane configuration, solid circles (●) indicate peaks belong to  $FMR_{\parallel}$  branch in 7 nm Fe, solid triangles (▼) indicate peaks belong to  $FMR_{\nparallel}$  branch in 7 nm Fe, hollow circles (○) indicate peaks belong to  $FMR_{\parallel}$  branch in 3 nm Fe, and hollow triangles (▽) indicate peaks belong to  $FMR_{\nparallel}$  branch in 3 nm Fe.

color scale as the indicator marks. We can identify the dispersion curve traced by the black solid line as originating from the 7 nm Fe layer and the curve traced by the grey solid line as originating from the 3 nm Fe layer. Both dispersion curves also have a  $FMR_{\parallel}$  branch and a  $FMR_{\nparallel}$  branch. Fig. 3(c) shows several typical curves measured in this configuration at various microwave frequencies between 3.8 GHz and 4.2 GHz. All the resonance peaks are dominated by Lorentz line shape, and we describe the key features by the following Eqs. (2):

At  $\varphi_H = 0^\circ, \vartheta_H \approx 90^\circ$  :

$$V(H) = V(-H) \quad (2a)$$

$$\frac{V_{Fe_7}}{|V_{Fe_7}|} = \frac{V_{Fe_3}}{|V_{Fe_3}|} \quad (2b)$$

$$\frac{V_{FMR_{\parallel}}}{|V_{FMR_{\parallel}}|} = \frac{V_{FMR_{\nparallel}}}{|V_{FMR_{\nparallel}}|} \quad (2c)$$

Equations (2) are quite different from Eqs. (1). Eq. (2a) shows the voltage signal keeps the same polarity when  $\mathbf{H}$  reverses, which indicates that spin pumping and the inverse spin hall effect are ignorable in our measurement<sup>20</sup>. Eq. (2b) shows the signal polarity in the two Fe layers are the same and Eq. (2c) shows the signal polarity in the  $FMR_{\nparallel}$  branch remains the same as in the  $FMR_{\parallel}$  branch. From Fig. (3) (c), the resonance peaks in the  $FMR_{\nparallel}$  branch are also much broader than those in the  $FMR_{\parallel}$  branch. Comparing Fig. (2) and (3), the SRE signal in the  $FMR_{\nparallel}$  branch has the same behavior as in the  $FMR_{\parallel}$  branch when changing the measurement configuration. The signal polarities in the two branches are opposite in the in-plane configuration, but same in the out-of-plane configuration.

So far, in the literature, the SRE has been systematically studied only in the configuration with  $\mathbf{M} \parallel \mathbf{H}$ , and the rectification voltage is described by a formula as a function of  $\mathbf{H}$ <sup>10</sup>. Since  $\mathbf{M}$  and  $\mathbf{H}$  are non-collinear in the  $FMR_{\nparallel}$  branch, the conclusions in previous studies

are not suitable here any more. However, the  $\mathbf{M}$  alignment is always parallel to the effective field  $\mathbf{H}_{eff}$  rather than  $\mathbf{H}$ . Thus,  $\mathbf{H}_{eff}$  instead of  $\mathbf{H}$  should be taken into account especially in ferromagnetic systems with strong anisotropy.  $\mathbf{H}_{eff}$  could be determined by the free energy  $F$  of the system. Considering the single crystal magnetic thin film in our case with Zeeman energy, magneto-crystalline anisotropy, shape anisotropy, one can get  $\mathbf{F}$  and  $\mathbf{H}_{eff}$  as follows:

$$F = -\mu_0 M H [\cos \theta_H \cos \theta_M \cos(\varphi_M - \varphi_H) + \sin \theta_H \sin \theta_M] + \frac{1}{2} \mu_0 M_{eff}^2 \sin^2 \theta_M + \frac{1}{4} K_1 (\sin^2 2\theta_M + \cos^4 \theta_M \sin^2 2\varphi_M) \quad (3a)$$

$$(\mu_0 H_{eff})^2 = \left( \frac{\omega}{\gamma} \right)^2 = \frac{\mu_0^2}{(\mu_0 M \cos \theta_M)^2} \left[ \frac{\partial^2 F}{\partial \theta_M^2} \frac{\partial^2 F}{\partial \varphi_M^2} - \left( \frac{\partial^2 F}{\partial \varphi_M \partial \theta_M} \right)^2 \right] \Bigg|_{(\theta_M, \varphi_M)} \quad (3b)$$

Here  $\mu_0$  is susceptibility in a vacuum,  $\mathbf{M}_{eff}$  is the effective moment, and  $K_1$  is the four-fold anisotropy constant.  $\varphi_M, \vartheta_M, \varphi_H$  and  $\vartheta_H$  are the angles of  $\mathbf{M}$  and  $\mathbf{H}$ , as defined in the insets of Fig. 4(a) and Fig. 5(a). **In the in-plane configuration,  $\vartheta_M = \vartheta_H = 0^\circ$ , so the effective field is:**

$$(\mu_0 H_{eff})^2 = [\mu_0 H \cos(\varphi_H - \varphi_M) + \mu_0 M_{eff} + \mu_0 H_1 - \frac{1}{2} \mu_0 H_1 \sin^2 2\varphi_M] * [\mu_0 H \cos(\varphi_H - \varphi_M) + \mu_0 H_1 \cos 4\varphi_M] \quad (4)$$

and in the out-of-plane configuration,  $\vartheta_H = 90^\circ, \varphi_M = \varphi_H = 0^\circ$ , so the effective field is:

$$(\mu_0 H_{eff})^2 = [\mu_0 H \sin \theta_M + \mu_0 M_{eff} \cos 2\theta_M + \mu_0 H_1 \cos 4\theta_M] * [\mu_0 H \cos \theta_H / \cos \theta_M + \mu_0 H_1 \cos^2 \theta_M] \quad (5)$$

**Here, and the four fold anisotropy  $\mu_0 H_1 = 2K_1/M$ .** Putting the effective field calculated from Eq. (4) and (5) together with the microwave field  $\mathbf{h}_{X'Y'Z'} = (0, h_{Y'} \cos(\delta) e^{i\omega t}, 0)$  into the LLG equation, we can get the dynamic magnetization  $\mathbf{m}$ . Here  $\delta$  is the phase of  $\mathbf{h}$ . In our system, we define  $\delta = 0$  in the 7 nm Fe and  $\delta = \pi$  in the 3 nm Fe. Spin rectification voltage can be calculated by  $V_{SR} = \langle j * \Delta R \rangle$ , here  $j$  is the microwave current in the system, and  $\Delta R \propto Re(m)$  is the resistance variation within the system due to AMR and spin precession. Thus we can derive the SRE in the in-plane configuration:

$$V_{SR} = A * Re(\chi_T) h_{Y'} \cos(\varphi_M + \delta) \sin(2\varphi_M) \quad (6)$$

and the SRE in the out-of-plane configuration:

$$V_{SR} = A * Re(\chi_L) h_{Y'} \sin(2\theta_M) \quad (7)$$

with

$$A = -\frac{j_{x'} \Delta R}{2M}$$

$$Re(\chi_L) = -\frac{\omega_M \omega_{H_{eff}} (\omega_{H_{eff}}^2 - \omega^2)}{(\omega_{H_{eff}}^2 - \omega^2)^2 + 4\omega_{H_{eff}}^2 \alpha^2 \omega^2}$$

$$Re(\chi_T) = \frac{2\alpha \omega^2 \omega_M \omega_{H_{eff}}}{(\omega_{H_{eff}}^2 - \omega^2)^2 + 4\omega_{H_{eff}}^2 \alpha^2 \omega^2}$$

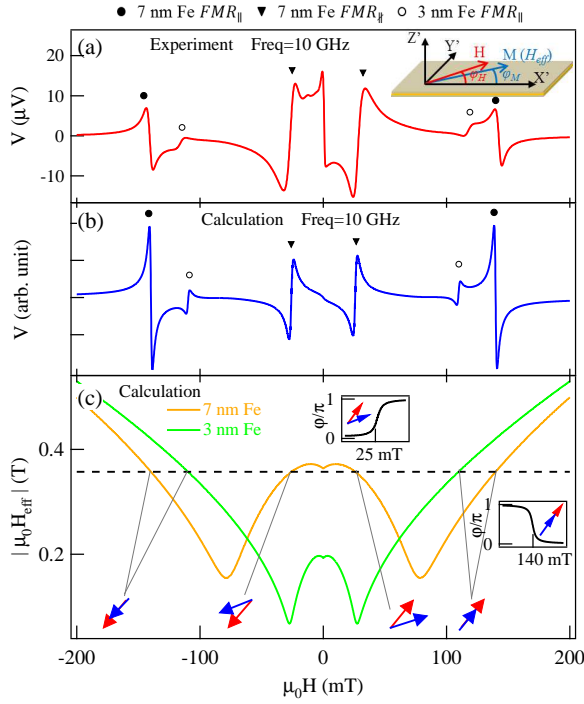


FIG. 4. Comparison of experiment and calculation results in the in-plane configuration. (a) Experiment curve with microwave frequency of 10 GHz, the inset shows a non-collinear configuration of  $\mathbf{M}$  and  $\mathbf{H}$  in the in-plane configuration. (b) Calculation curve with microwave frequency fixed at 10 GHz, the result agrees with Eqs. (1). Solid lines in (c) are the calculated effective field as a function of the applied field of the 7 nm Fe layer and 3 nm Fe layer in the in-plane configuration and the dashed line indicates the position of the effective field which satisfies resonance conditions at a microwave frequency of 10 GHz. The insets are the calculated spin resonance phase  $\varphi$  in the  $FMR_{||}$  and the  $FMR_{\perp}$  branches in 7 nm Fe.

Here  $j_{x'}$  is the microwave current amplitude,  $\text{Re}(\chi_L)$  and  $\text{Re}(\chi_T)$  are respectively the real parts of the diagonal and non-diagonal elements of the dynamic susceptibility tensor,  $\omega$  is the applied microwave frequency,  $\omega_M = \gamma M$ ,  $\omega_{H_{eff}} = \gamma H_{eff}$ ,  $\gamma$  is the gyromagnetic ratio, and  $\alpha$  is the damping constant. **The experiment data in Fig. 2 and 3 show that the relative phase  $\Phi$  between  $\mathbf{h}$  and  $\mathbf{j}$  is almost an integer of  $\pi$ . To simplify the situation, we fix the relative phase  $\Phi$  as an integer of  $\pi$  in our calculation, thus only the real part of  $\chi$  will contribute to the signal voltage, as discussed by M. Harder et al.<sup>14</sup>** As shown in Eq. (6) and (7),  $V_{SR}$  depends on  $\mathbf{H}_{eff}$  instead of  $\mathbf{H}$ , and cannot directly calculated by a simple formula. To analyze the SRE, we first get  $\varphi_M$  and  $\vartheta_M$  as functions of  $\mathbf{H}$  by minimizing the system Free energy  $F$  in Eq. (3a), then calculate  $\mathbf{H}_{eff}$  with Eq. (3b), and finally calculate  $V_{SR}$  using Eq. (6) and (7).

Figure 4 shows a comparison between calculation and experimental results in the in-plane configuration. Fig. 4(a) is a typical experimental curve measured at a microwave frequency of 10 GHz, and (b) shows the cal-

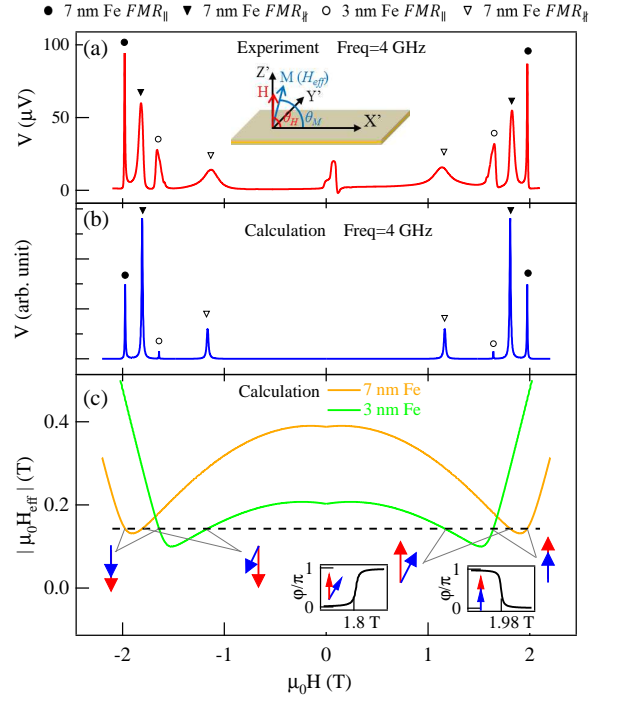


FIG. 5. Comparison of experiment and calculation results in the out-of-plane configuration. (a) Experiment curve with microwave frequency of 4 GHz, the inset shows a non-collinear configuration of  $\mathbf{M}$  and  $\mathbf{H}$  in the out-of-plane configuration. (b) Calculation curve with microwave frequency fixed at 4 GHz, the result agrees with Eqs. (2). Solid lines in (c) are the calculated effective field as a function of the applied field of the 7 nm Fe layer and 3 nm Fe layer in the out-of-plane configuration and the dashed line indicates the position of the effective field which satisfies resonance conditions at a microwave frequency of 4 GHz. The insets are the calculated spin resonance phase  $\varphi$  in the  $FMR_{||}$  and the  $FMR_{\perp}$  branches in 7 nm Fe.

culated curve with the microwave frequency fixed at 10 GHz, the effective field  $\mathbf{H}_{eff}$  as a function of  $\mathbf{H}$  in the in-plane configuration is shown in (c). In the calculation, we use  $\varphi_H = 44.6^\circ$  and  $\vartheta_H = 0^\circ$  for the in-plane configuration,  $\mu_0 H_1 = 73 \text{ mT}$ ,  $\mu_0 M_{eff} = 1.7 \text{ T}$  for 7 nm Fe, and  $\mu_0 H_1 = 26 \text{ mT}$ ,  $\mu_0 M_{eff} = 1.4 \text{ T}$  for 3 nm Fe. All these parameters are determined from the dispersion curves in Fig. 2(b). We use  $\alpha = 0.006$  determined from the experimental linewidth of the resonance, and set  $A_{Fe_7} = 5 \times A_{Fe_3}$  to best represent the experimental conditions. The calculation results agree well with the experimental results. From Eq. (6),  $V_{SR}$  is determined by the real part of the diagonal elements of the dynamic susceptibility tensor  $\text{Re}(\chi_L)$  which has an anti-symmetric Lorentz lineshape, so  $V_{SR}$  has anti-symmetric Lorentz lineshape as shown in Fig. 4(b), in good agreement with experimental result. Since  $V_{SR} \propto \cos(\varphi_M + \delta) \sin(2\varphi_M)$ , and when  $\mathbf{H}$  reverses, the  $\mathbf{H}_{eff}$  and  $\mathbf{M}$  will reverse, which corresponds to  $\varphi_M + \pi$  and  $\vartheta_M + \pi$ ,  $V_{SR}$  will change its polarity when  $\mathbf{H}$  reverses as shown in Fig. 4(b) and agrees with Eq. (1a).  $V_{SR}$  has the opposite polarity in

the 7 nm Fe layer and the 3 nm Fe layer, as shown in Fig. 4(b) and confines with Eq. (1b), because the phase  $\delta$  of the rf field  $\mathbf{h}$  in these two Fe layers has a difference of  $\pi$ . Near the resonance field as indicated by the dashed line in Fig. 4(c),  $(H - H_0) / (H_{eff} - H_0) > 0$  in the  $FMR_{\parallel}$  branch, while  $(H - H_0) / (H_{eff} - H_0) < 0$  in the  $FMR_{\perp}$  branch, here  $H_0$  is the resonance field. Since the sign of  $V_{SR}$  is determined by  $(\omega_{H_{eff}}^2 - \omega^2)$ , the  $V_{SR}$  H curve has the opposite polarity in the  $FMR_{\parallel}$  and the  $FMR_{\perp}$  branch, in good agreement with the experiment in Fig. 4(b) as well as with Eq. (1c). Thus, the agreement between experiment and calculation in our system verifies that the approximation of the relative phase  $\Phi$  as an integer of  $\pi$  is reasonable. If the relative phase  $\Phi$  shifts from an integer of  $\pi$ , the imaginary part of the dynamic susceptibility  $\chi$  will contribute to the voltage signal and contribute a Lorentz component to the curve, as discussed by M. Harder et al.<sup>14</sup>. Moreover, if the Lorentz component is much larger than the anti-symmetric Lorentz component, the overall lineshape will be Lorentz, and the signal polarity will be similar to that in the out-of-plane configuration we will discuss in the following.

In the out-of-plane configuration, our theory also works well. Fig. 5 shows a comparison between calculation and experimental results in the out-of-plane configuration. Fig. 5(a) is a typical experimental curve measured at a microwave frequency of 4 GHz, and (b) shows the calculated curve with the microwave frequency of 4 GHz. Fig. 5(c) shows the calculated effective field  $\mathbf{H}_{eff}$  as a function of  $\mathbf{H}$ . In our calculation, we use  $\varphi_H = 0^\circ$  and  $\vartheta_H = 89.4^\circ$  for the out-of-plane configuration, and keep the other parameters the same as those used in the in-plane configuration. Eq. (7) shows that  $V_{SR}$  is determined by the real part of the non-diagonal elements of the dynamic susceptibility tensor  $\text{Re}(\chi_T)$  and has a Lorentz line shape, which can be proved by the calculated curve in Fig. (5)(b), and agrees with experimental results. Since  $V_{SR} \propto \sin(2\theta_M)$ ,  $V_{SR}$  keeps the same polarity when  $\mathbf{H}$  reverses (agrees with Eq. (2a)), and keeps the same polarity in the 7 nm Fe and the 3 nm Fe layer (agrees with Eq. (2b)). Eq. (7) shows that the sign of  $V_{SR}$  is determined by  $\omega_{H_{eff}}$ , so the  $V_{SR}$  polarity remains the same in the  $FMR_{\parallel}$  branch and the  $FMR_{\perp}$  branch.

We further calculated the spin resonance phase  $\varphi$  in both in-plane and out-of-plane configuration, and the calculated  $\varphi$  in the 7 nm Fe are shown in insets in Fig. 4(c) and 5(c) respectively. The spin resonance phase  $\varphi$  describes the phase lag between the precessing magnetization and the driving microwave field, and can be determined by  $\cos \varphi = \text{Re}(\chi) / |\chi|$ <sup>10,14,37</sup>. Shown in insets in Fig. 4(c) and 5(c), in collinear configuration,  $\varphi = \pi$  when  $H < H_0$ , which is called a driving force out of phase, and  $\varphi = 0$  when  $H > H_0$  which is called a driving force in phase.  $\varphi$  will change from  $\pi$  to 0 as H increases around FMR and  $\varphi = \pi/2$  at FMR, here we define such a phase jump as a negative phase jump. While in non-collinear configuration,  $\varphi = 0$  (driving force in phase) when  $H < H_0$ , and  $\varphi = \pi$  (driving force out of phase)

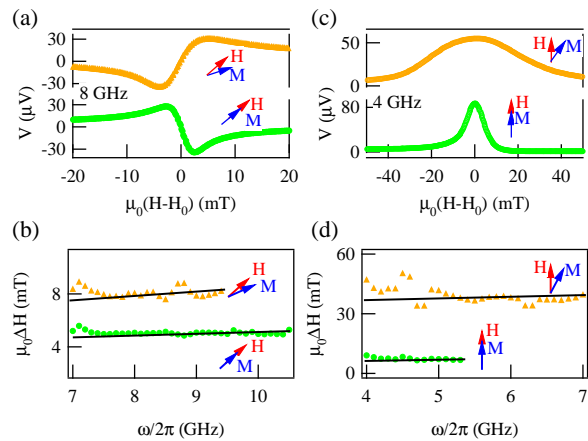


FIG. 6. (a) The rectification voltage and (b) the linewidth in the 7 nm Fe in the  $FMR_{\parallel}$  branch and the  $FMR_{\perp}$  branch as a function of  $H - H_0$  in in-plane configuration, and (c) the rectification voltage and (d) the linewidth in the out-of-plane configuration. The black lines are guide lines for the eyes.

when  $H > H_0$ .  $\varphi$  will change from 0 to  $\pi$  as H increases around FMR and  $\varphi = \pi/2$  at FMR, here we define such a phase jump as a positive phase jump. Considering the effective field as shown in Fig. 4(c) and 5(c) rather than the applied field, in both collinear and non-collinear configuration, the phase  $\varphi$  is  $\pi$  when  $H_{eff} < H_0$ , and is 0 when  $H_{eff} > H_0$ . And  $\varphi$  changes from  $\pi$  to 0 as  $H_{eff}$  increases around FMR and  $\varphi = \pi/2$  at FMR, which means the phase jump is negative in both collinear and non-collinear configuration by considering the effective field. So in both in-plane and out-of-plane configurations, as H increases, the phase  $\varphi$  between the spin precession and the driving microwave magnetic field decreases in the collinear configuration and increases in the non-collinear configurations at FMR, and the difference is due to the different H-dependence effective field in collinear and non-collinear configuration.

The calculation and the experimental results of the SRE in the 7 nm Fe layer are listed in Table I. Our theory well describes the line shape and polarity of the SRE in the general configuration of  $\mathbf{M}$  and  $\mathbf{H}$ . Also our calculation qualitatively confirms the broadening of the linewidth  $\Delta H$  for non-collinear alignment of  $\mathbf{M}$  and  $\mathbf{H}$ . However, the experimental value of the linewidth is much broader than the calculated results, and the linewidth broadening in the non-collinear configuration in the experiment is also much larger than that in theory. In our theory, the effect of the interface on FMR hasn't been taken into account, however, it is known that some interfacial effects, such as spin pumping, magnon scattering<sup>10,26,27,38</sup>, will enhance the linewidth.

Fig. 6 directly compares the linewidth in the collinear and non-collinear configuration. The rectification voltage in the  $FMR_{\parallel}$  branch and the  $FMR_{\perp}$  branch are plotted against their resonance field  $H - H_0$  in the in-plane configuration as shown in Fig. 6(a). The full width at half maximum  $\delta H$  of FMR at different microwave frequen-

	Measurement Configuration	Line shape	polarity	$\mu_0 H_0$ (T)	$\mu_0 \Delta H$ (mT)
M $\parallel$ H	$\varphi_H = 44.6^\circ, \vartheta_H = 0^\circ, f = 10$ GHz	Anti-Lorentz <sub>(Exp)</sub>	- <sub>(Exp)</sub>	0.14 <sub>(Exp)</sub>	5.3 <sub>(Exp)</sub>
		Anti-Lorentz <sub>(Cal)</sub>	- <sub>(Cal)</sub>	0.14 <sub>(Cal)</sub>	2.4 <sub>(Cal)</sub>
	$\varphi_H = 0^\circ, \vartheta_H = 89.4^\circ, f = 4$ GHz	Lorentz <sub>(Exp)</sub>	+ <sub>(Exp)</sub>	1.96 <sub>(Exp)</sub>	9.5 <sub>(Exp)</sub>
		Lorentz <sub>(Cal)</sub>	+ <sub>(Cal)</sub>	1.97 <sub>(Cal)</sub>	7.2 <sub>(Cal)</sub>
M $\nparallel$ H	$\varphi_H = 44.6^\circ, \vartheta_H = 0^\circ, f = 10$ GHz	Anti-Lorentz <sub>(Exp)</sub>	+ <sub>(Exp)</sub>	0.027 <sub>(Exp)</sub>	10 <sub>(Exp)</sub>
		Anti-Lorentz <sub>(Cal)</sub>	+ <sub>(Cal)</sub>	0.026 <sub>(Cal)</sub>	3.6 <sub>(Cal)</sub>
	$\varphi_H = 0^\circ, \vartheta_H = 89.4^\circ, f = 4$ GHz	Lorentz <sub>(Exp)</sub>	+ <sub>(Exp)</sub>	1.79 <sub>(Exp)</sub>	54 <sub>(Exp)</sub>
		Lorentz <sub>(Cal)</sub>	+ <sub>(Cal)</sub>	1.80 <sub>(Cal)</sub>	13 <sub>(Cal)</sub>

TABLE I. The calculation and the experimental results of the SRE in the  $\mathbf{M} \parallel \mathbf{H}$  and the  $\mathbf{M} \nparallel \mathbf{H}$  configuration in 7 nm Fe layer with different measurement geometry. The positive polarity of the SRE is defined as  $V_{SR}/|V_{SR}| > 0$  when  $H < H_0$ . The subscript Exp indicates the result is extracted from the experimental data, and the subscript Cal indicates the result is extracted from the calculation data.

cies are plotted in Fig. 6(b), which clearly shows the broadening of linewidth in the non-collinear configuration. Besides the in-plane configuration, the linewidth in the out-of-plane configuration is also analyzed, and shown in Fig. 6 (c) and (d). The linewidth of non-collinear resonance is much broader than that of collinear resonance for the out-of-plane configuration. In

our theory, the Fe layers are only treated as a single domain, but in the non-collinear configuration, the magnetization is not saturated and might form the multi-domain, which may cause magnetization inhomogeneous and lead to an additional damping<sup>39</sup>. Nevertheless, this is still an open question for further study.

In conclusion, we studied the spin rectification effect in an epitaxial Fe/Au/Fe tri-layer system with strong magneto anisotropy and shape anisotropy. In addition to the SRE when  $\mathbf{M}$  and  $\mathbf{H}$  are collinear, we study  $V_{SR}$  for the case where  $\mathbf{M}$  and  $\mathbf{H}$  are non-collinear. The different behavior of  $V_{SR}$  in different configurations of  $\mathbf{M}$  and  $\mathbf{H}$  are due to the relationship between  $\mathbf{H}_{eff}$  and  $\mathbf{H}$ . By considering  $\mathbf{H}_{eff}$  instead of  $\mathbf{H}$  in ferromagnetic systems, we extend the SRE theory for all  $\mathbf{M}$  and  $\mathbf{H}$  configurations. These equations will help further the understanding of

spin transport in ferromagnetic systems, especially for  $\mathbf{M}$  not parallel to  $\mathbf{H}$ .

**Acknowledgments** This project was supported by the National Key Basic Research Program (Grants No. 2015CB921401 and No. 2011CB921801), National Science Foundation (Grants No. 11274074, 11434003, 11474066 and 11429401) of China, and NSERC grants. The authors thank J. X. Li from Fudan University, Z. H. Zhang, B. M. Yao, L. Fu and Y. S. Gui from University of Manitoba, and X. L. Fan from Lanzhou University.

\* 11110190012@fudan.edu.cn

<sup>1</sup> A. A. Tulapurkar, Y. Suzuki, A. Fukushima, H. Kubota, H. Maehara, K. Tsunekawa, D. D. Djayaprawira, N. Watanabe, and S. Yuasa, Nature (London) **438**, 339 (2005).

<sup>2</sup> J. C. Sankey, P. M. Braganca, A. G. F. Garcia, I. N. Krivorotov, R. A. Buhrman, and D. C. Ralph, Phys. Rev. Lett. **96**, 227601 (2006).

<sup>3</sup> Y. S. Gui, S. Holland, N. Mecking, and C.-M. Hu, Phys. Rev. Lett. **95**, 056807 (2005).

<sup>4</sup> S. T. Goennenwein, S. W. Schink, A. Brandlmaier, A. Boger, M. Opel, R. Gross, R. S. Keizer, T. M. Klapwijk, A. Gupta, H. Huebl, C. Bihler, and M. S. Brandt, Appl. Phys. Lett. **90**, 162507 (2007).

<sup>5</sup> A. Azevedo, L. H. Vilela Leão, R. L. Rodriguez-Suarez, A. B. Oliveira, and S. M. Rezend, J. Appl. Phys. **97**, 10C715 (2005).

<sup>6</sup> E. Saitoh, M. Ueda, H. Miyajima, and G. Tatara, Appl. Phys. Lett. **88**, 182509 (2006).

<sup>7</sup> M. V. Costache, S. M. Watts, M. Sladkov, C. H. van der Wal, and B. J. van Wees, Appl. Phys. Lett. **89**, 232115 (2006).

<sup>8</sup> Y. S. Gui, N. Mecking, X. Zhou, G. Williams, and C.-M. Hu, Phys. Rev. Lett. **98**, 107602 (2007).

<sup>9</sup> A. Yamaguchi, H. Miyajima, T. Ono, Y. Suzuki, S. Yuasa, A. Tulapurkar, and Y. Nakatani, Appl. Phys. Lett. **90**, 182507 (2007).

<sup>10</sup> N. Mecking, Y. S. Gui, and C.-M. Hu, Phys. Rev. B **76**, 224430 (2007).

<sup>11</sup> T. Moriyama, R. Cao, X. Fan, G. Xuan, B. K. Nikoli, Y. Tserkovnyak, J. Kolodzey, and J. Q. Xiao, Phys. Rev. Lett. **100**, 067602 (2008).

<sup>12</sup> H. Xiong, A. Wirthmann, Y. S. Gui, Y. Tian, X. F. Jin,

- Z. H. Chen, S. C. Shen, and C.-M. Hu, *Appl. Phys. Lett.* **93**, 232502 (2008).
- <sup>13</sup> O. Mosendz, J. E. Pearson, F.Y. Fradin, G. E.W. Bauer, S. D. Bader, and A. Hoffmann, *Phys. Rev. Lett.* **104**, 046601 (2010).
- <sup>14</sup> M. Harder, Z. X. Cao, Y. S. Gui, X. L. Fan, and C.-M. Hu, *Phys. Rev. B* **84**, 054423 (2011).
- <sup>15</sup> A. Azevedo, L. H. Vilela-Leão, R. L. Rodríguez-Suárez, A. F. Lacerda Santos, and S. M. Rezende, *Phys. Rev. B* **83**, 144402 (2011).
- <sup>16</sup> Z. Feng, J. Hu, L. Sun, B. You, D.Wu, J. Du, W. Zhang, A. Hu, Y. Yang, D. M. Tang, B. S. Zhang, and H. F. Ding, *Phys. Rev. B* **85**, 214423 (2012).
- <sup>17</sup> L. Chen, F. Matsukura, and H. Ohno, *Nat. Commun.* **4**, 2055 (2013).
- <sup>18</sup> E. Th. Papaioannou, P. Fuhrmann, M. B. Jungfleisch, T. Brächer, P. Pirro, V. Lauer, J. Lösch, and B. Hillebrands, *Appl. Phys. Lett.* **103**, 162401 (2013).
- <sup>19</sup> H. Chen, X. Fan, W. Wang, H. Zhou, Y. S. Gui, C.-M. Hu, and D. Xue, *Appl. Phys. Lett.* **102**, 202410 (2013).
- <sup>20</sup> L. H. Bai, P. Hyde, Y. S. Gui, C.-M. Hu, V. Vlainck, J. E. Pearson, S. D. Bader, and A. Hoffmann, *Phys. Rev. Lett.* **111**, 217602 (2013).
- <sup>21</sup> M. Obstbaum, M. Härtinger, H. G. Bauer, T. Meier, F. Swientek, C. H. Back, and G. Woltersdorf, *Phys. Rev. B* **89**, 060407(R) (2014).
- <sup>22</sup> P. Hyde, L. H. Bai, D. M. J. Kumar, B. W. Southern, C.-M. Hu, S. Y. Huang, B. F. Miao, and C. L. Chien, *Phys. Rev. B* **89**, 180404(R) (2014).
- <sup>23</sup> J. Kleinlein, B. Ocker, and G. Schmidt, *Appl. Phys. Lett.* **104**, 153507 (2014).
- <sup>24</sup> Y. S. Gui, L. H. Bai, and C.-M. Hu, *Sci. China-Phys. Mech. Astron.* **56**, 124 (2013).
- <sup>25</sup> L. H. Bai, Y. S. Gui, and C.-M. Hu, in *Introduction to Spintronics*, edited by X. F. Han, et al (Science Press, Beijing, 2014), Chapter 9 (in chinese).
- <sup>26</sup> B. Heinrich, C. Burrowes, E. Montoya, B. Kardasz, E. Girt, Y.-Y. Song, Y. Sun, and M. Wu, *Phys. Rev. Lett.* **107**, 066604 (2011).
- <sup>27</sup> J.-C. Rojas-Sánchez, N. Reyren, P. Laczkowski, W. Savero, J.-P. Attan, C. Deranlot, M. Jamet, J.-M. George, L. Vila, and H. Jaffrs, *Phys. Rev. Lett.* **112**, 106602 (2012).
- <sup>28</sup> G. Counil, Joo-Von Kim, T. Devolder, P. Crozat, C. Chappert, and A. Cebollada, *J. Appl. Phys.* **98**, 023901 (2005).
- <sup>29</sup> H. Ohta, S. Imagawa, M. Morokawa, and E. Kita, *J. Phys. Soc. Jpn.* **62**, 4467 (1993).
- <sup>30</sup> G. Chen, J. X. Li, J. Zhu, J. H. Liang, and Y. Z. Wu, *J. Appl. Phys.* **109**, 07C108 (2011).
- <sup>31</sup> P. Grünberg, R. Schreiber, Y. Pang M. B. Brodsky and H. Sowers, *Phys. Rev. Lett.* **57**, 2442 (1986).
- <sup>32</sup> A. Layadi and J.O. Artman, *J. Magn. Magn. Mater.* **92**, 143 (1990).
- <sup>33</sup> Y. Chen, X. Fan, Y. Zhou, Y. Xie, J. Wu, T. Wang, S. T. Chui, J. Q. Xiao, *Adv. Mater.* **27**, 1351 (2015).
- <sup>34</sup> X. M. Liu, Hoa T. Nguyen, J. Ding, M. G. Cottam, and A. O. Adeyeye, *Phys. Rev. B* **90**, 064428 (2014).
- <sup>35</sup> Bret Heinrich, Yaroslav Tserkovnyak, GeorgWoltersdorf, Arne Brataas, Radovan Urban, and Gerrit E.W. Bauer, *Phys. Rev. Lett.* **90**, 187601 (2003).
- <sup>36</sup> X. F. Zhu, M. Harder, J. Tayler, A. Wirthmann, B. Zhang, W. Lu, Y. S. Gui, and C.-M. Hu, *Phys. Rev. B* **83**, 140402(R) (2011).
- <sup>37</sup> A. Wirthmann, X. L. Fan, Y. S. Gui, K. Martens, G. Williams, J. Dietrich, G. E. Bridges, and C.-M. Hu, *Phys. Rev. Lett.* **105**, 017202 (2010).
- <sup>38</sup> R. Urban, G. Woltersdorf, and B. Heinrich, *Phys. Rev. Lett.* **87**, 217204 (2001).
- <sup>39</sup> Shufeng Zhang and Steven S.-L. Zhang, *Phys. Rev. Lett.* **102**, 086601 (2009)